Supplementary Information

Pre-constructing a mortice-tenon joint based-layer to achieve an enhanced SEI on Li metal anode

Kun Wang, [a] Cutao Wang, [a] Sheng Liu, [a] Congcong Du, [b] Qingyi Zheng, [a] Jiaqing Cui, [a] Xinxin Yang, [b] Yuxin Tang, [a] Ruming Yuan, [a] Mingsen Zheng, [a] Jingmin Fan*[a] and Quanfeng Dong*[a]

Fabrication of the based-layer (DFSA-Li) anode

The fabrication of based-layer anodes was carried out in an argon-filled glove box (O_2 <0.1 ppm, H_2O < 0.1 ppm). 4 vol% of 2-(Fluorosulphonyl)difluoroacetic acid (DFSA, 98%, Energy-Chemical) was added into dimethyl ether (DME, 99.9%, DoDoChem) to form uniform solutions. Subsequently, 80 μL of the above solution was dropped on the surface of a lithium foil (15.6 mm in diameter) for a certain time at room temperature and then washed with DME for over 3 times to remove the remaining DFSA. The prepared based-layer anode was cut into 12 mm discs for further use. The fabrication method for the based-layer on Cu collectors was the same, except that the former used different deposition amounts of Li.

Preparation of the electrolyte

Two basic electrolytes were used in this study (FEC-based carbonate electrolyte and commercial carbonate electrolyte). The applied FEC-based carbonate electrolyte was dissolved 1 M lithium hexafluorophosphate ($LiPF_6$, 99.9%, DoDoChem) into fluoroethylene carbonate (FEC, 99.9%, DoDoChem) and ethyl methyl carbonate (EMC, 99.9%, DoDoChem) with v/v=3:7, if not specifically stated. The commercial carbonate electrolyte consisted of 1 M $LiPF_6$ in ethylene carbonate EC/EMC with v/v=3:7 (LB-224, 99.9%, DoDoChem). For the TSFSA electrolyte, 2 vol% trimethylsilyl 2-(fluorosulphonyl)difluoroacetate (TSFSA, 95%, Leyan) was added into the two basic electrolytes to obtain the TSFSA electrolyte.

Material characterization

The SEM images of Li metal wereobserved by field emission scanning electron microscopy (SEM, HITACHI S-4800). The AFM images were tested by atomic force microscopy (AFM, SPM 5500; Keysight Technologies, Santa Rosa, CA, USA). The contact angles were determined using SL250 contact angle goniometer (U.S. KINO Company). The morphology/HRTEM/SAED/Mapping of SEI was characterized by transmission electron microscope (JEM 200F) with frozen sample rod (Fischione 2550). X-ray diffraction (XRD) was conducted using a Rigaku Ultima IV X-ray diffractometer based on Cu Kα radiation (λ = 1.5418 Å). Fourier transform infrared spectroscopy (FTIR) experiments were conducted by using a Nicolet iS50 FTIR spectrophotometer. X-ray photoelectron spectroscopy (XPS) was obtained by using PHI QUAN-TUM 2000. Time-of-flight secondary ion mass spectrometry was conducted using a PHI nanoTOF II Time-of-Flight SIMS (30 keV, 2 nA, Ion species: Bi^{3++}). The contact angles were tested the SL250 contact angle measuring instrument (KINO Company, USA). In-situ optical devices for in-situ optical characterization was designed as shown in Supplementary Fig. S23. The Li foils were used with a thickness of 300 μm.

Computational Details

The DFT calculations were performed at the B3LYP/6-311+G (d, p) level using Gaussian 09 and

GaussView 5.0 software. EC, EMC, FEC, $LiPF_6$, DFSA-Li and TFSFA molecules were optimized using the B3LYP hybrid functional. Ab initio molecular dynamics (AIMD) simulations were carried out by using Perdew-Burke-Ernzerhof (PBE) gradient-corrected exchange-corrected functional with the projector augmented plane wave (PAW) method as implemented in the Vienna ab-initio simulation package (VASP). The plane wave kinetic energy cutoff was set to 400 eV. NVT ensemble was used at 300 K with a time step of 1 fs.

Electrochemical characterization

For the four research systems, BE was used basic electrolyte without any improvement, based-layer was used DFSA-Li as Li anode and basic electrolyte and ESEI was used based-layer as Li anode and 2 vol% TSFSA as electrolyte. Li||Li symmetric cells (CR-2025 coin cells), Li-Cu half cells (CR-2016 coin cells), Li||LFP full cells (CR-2016 coin cells) and Li||NCM811 full cells (CR-2016 coin cells) were both assembled using a Celgard 2025 separator (19 mm in diameter). The electrolyte was controlled 35 μL for each cell. For the Li||LFP coin cells, the mass loading of the LFP cathode was 20.5 mg cm^{-2}, and the area capacity of Li anode was deposited 3 mAh cm^{-2} and 10 mAh cm^{-2} with basic FEC-based electrolyte or TSFSA electrolyte (the above capacities excluded the loss of the chemical reaction). The voltage windows for the Li||LFP full cells were set to 2.5-4.2 V. For the high-voltage Li||NCM811 full cells, the mass loading of the NCM811 cathode was 26.0 mg cm^{-2}, and the area capacity of Li anode was deposited 10 mAh cm^{-2} with TSFSA electrolyte (the above capacities excluded the loss of the chemical reaction). The voltage windows for the Li||NCM811 full cells were set to 2.8-4.6 V.

Cells galvanostatically charge and discharge tests were uesd the NEWARE BTS-5 V 5/20 mA (Shenzhen NEWARE). Electrochemical impedance spectra (EIS) were performed by Autolab PGSTAT204 with a test range of 1 MHz to 0.1 Hz. CV and Tafel curves were obtained by an electrochemical workstation (CHI 660E) using coin cells.

To evaluate the average CE of ESEI and based-layer, Cu foil pre-deposited with 1 mAh cm^{-2} Li were treated with DFSA and assembled Li-Cu half cells. First, completely stripping the Li metal on Cu foils. Then, redeposited 5 mAh cm^{-2} Li on Cu foil at a current density of 1 mA cm^{-2} and deposited/stripped 10 times at a capacity of 1 mAh cm^{-2}. After n cycles, the remaining Li was completely stripped to the cut-off voltage. The average CE over n cycles can be calculated by measuring the capacity of Li remaining after cycling with the equation:

$$Average\ CE = \frac{nQ_C + Q_S}{nQ_C + Q_{Li}} \quad (1)$$

where Q_C was the deposition and stripping capacity per cycle. Q_s was the final stripped capacity of Li remaining after n cycles and Q_{Li} was the initial deposited capacity of Li. Herein, the value of Q_{Li} was 5 mAh cm^{-2} and Q_C was 1 mAh cm^{-2}.

The method to obtain the activation energy (Ea) of Li deposition was as follows. EIS tests with Li||Li symmetric cells at different temperatures were carried out. Ea can be obtained by the following equation:

$$\frac{1}{R_{SEI}} = A_0 e^{-E_a/RT} \quad (2)$$

where R_{SEI}, A_0 and R represent the resistance of SEI, pre-exponential constant, the standard gas constant and the activation energy, respectively. Therefore, Ea can be obtained from the slope plot of log R_{SEI} vs. T^{-1}.

To obtain the lithium-ion diffusion coefficient of BE, based-layer and ESEI, CV tests were conducted at different scan speeds (0.1 mV s^{-1}-0.5 mV s^{-1}) using the Li||LFP full cells. The lithium-ion diffusion coefficient was obtained by fitting the Randles-Sevcik equation:

$$I_P = 0.4463nFAC_x v^{1/2}\sqrt{\frac{nFD_x}{RT}} \quad (3)$$

where I_P, n, A, D_x, v and C_x represent peak current, number of electrons in electrode reaction, electrode area, ion diffusion coefficient, scan rate and lithium-ion concentration.

Supplementary Figures

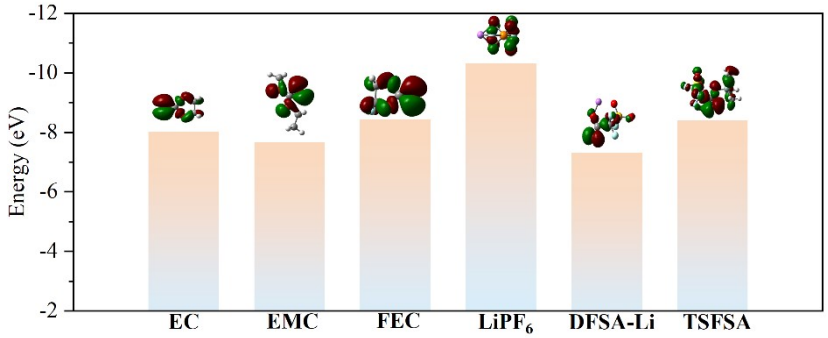

Fig. S1. HOMO energy level diagrams of the investigated salts ($LiPF_6$), solvents (EC, EMC and FEC), DFSA-Li and TSFSA.

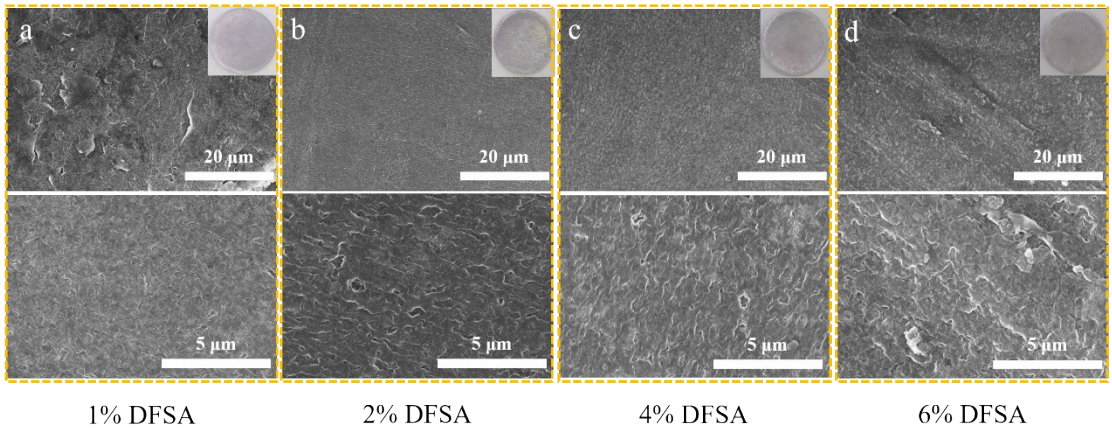

Fig. S2. The SEM images of DFSA-Li surface with different treatment concentration: (a) 1%, (b) 2%, (c) 4% and (d) 6%.

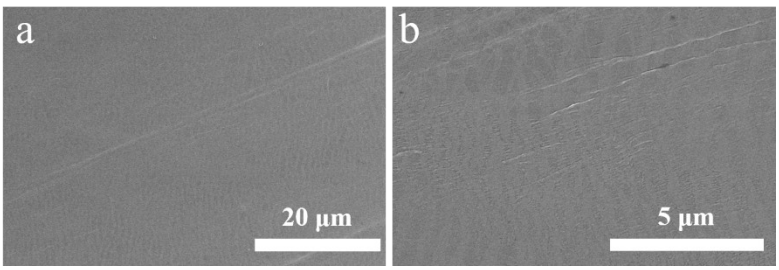

Fig. S3. The SEM images of Bare-Li surface.

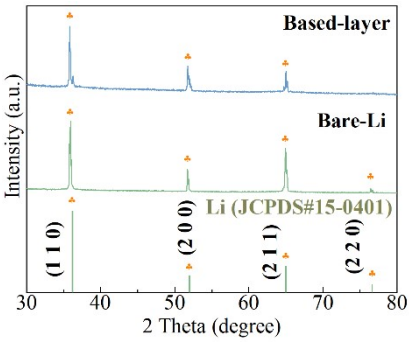

Fig. S4. XRD patterns of based-layer and bare-Li.

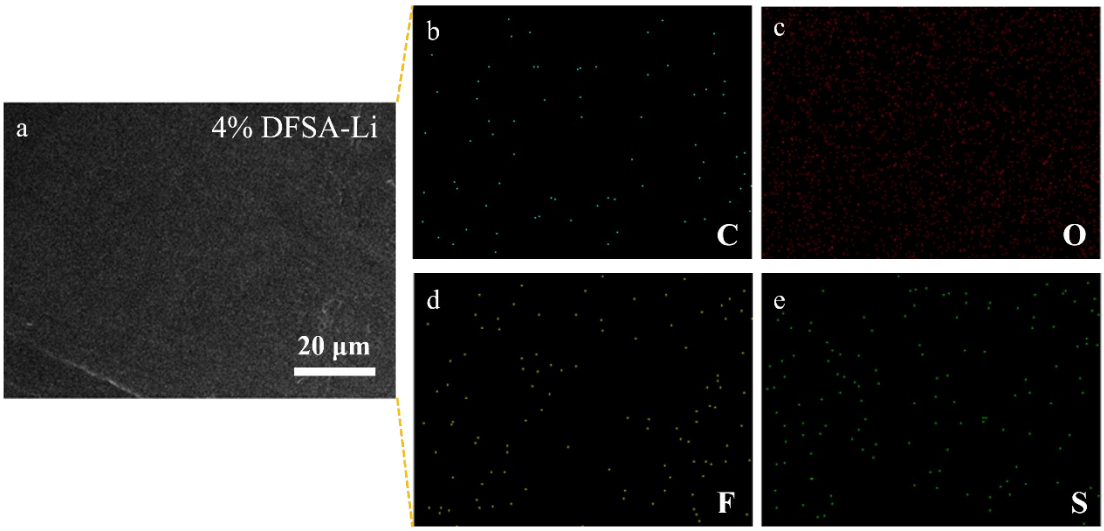

Fig. S5. (a) The SEM images of the surface of based-layer. (b-e) The corresponding energy dispersive spectroscopy (EDS) mapping (carbon, oxygen, fluorine and sulfur) in the same area.

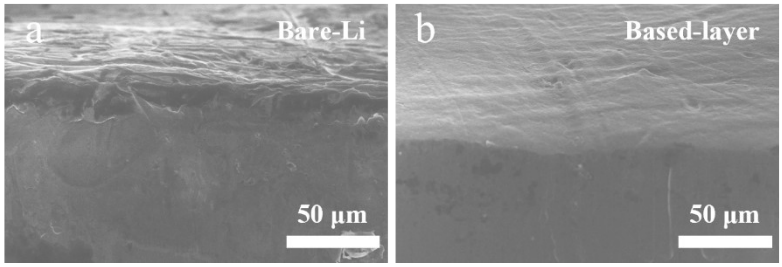

Fig. S6. The cross-sectional SEM images of (a) Bare-Li and (b) based-layer.

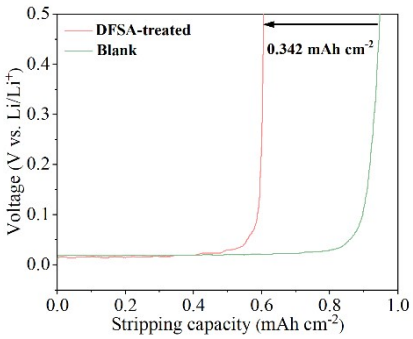

Fig. S7. Capacity-voltage curves of Li||Cu half cells with DFSA-treated Li on Cu foil and bare Cu foil. To determine the active Li capacities consumed by the displacement reaction, a Cu electrode pre-deposited with 1 mAh cm^{-2} of Li metal was selected as the target for the reaction. After reassembling the Li||Cu half-cell, all stripped Li capacity was 0.604 mAh cm^{-2}, indicating that approximately 0.342 mAh cm^{-2} of active Li was consumed by DFSA (4%). This consumption has a negligible impact on energy densities.

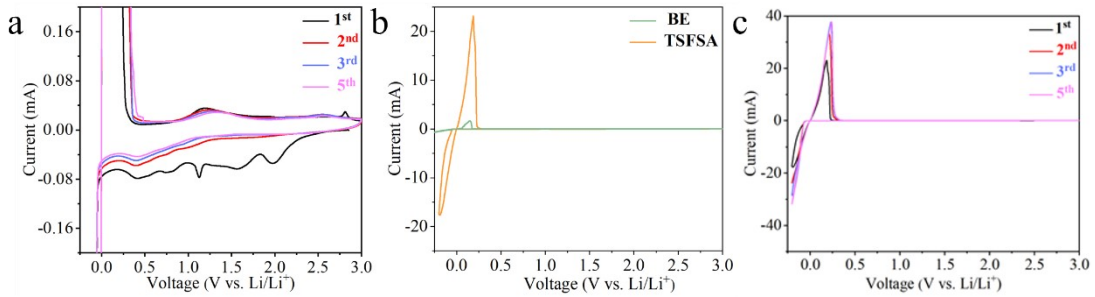

Fig. S8. (a) CV profiles scanned at -0.2-3 V of 1 mV s^{-1} in TSFSA electrolyte. (b) The first cycle CV profiles of BE and TSFSA with FEC-based carbonate electrolyte (1 M $LiPF_6$ in FEC/EMC, v/v=3:7). (c) CV profiles scanned at - 0.2-3 V of 1 mV s^{-1} in TSFSA electrolyte.

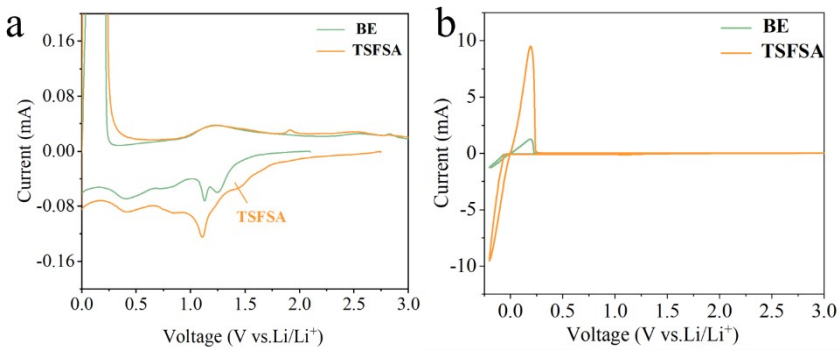

Fig. S9. The first cycle CV profiles of BE and TSFSA in commercial carbonate electrolyte (1 M $LiPF_6$ in EC/EMC, v/v=3:7).

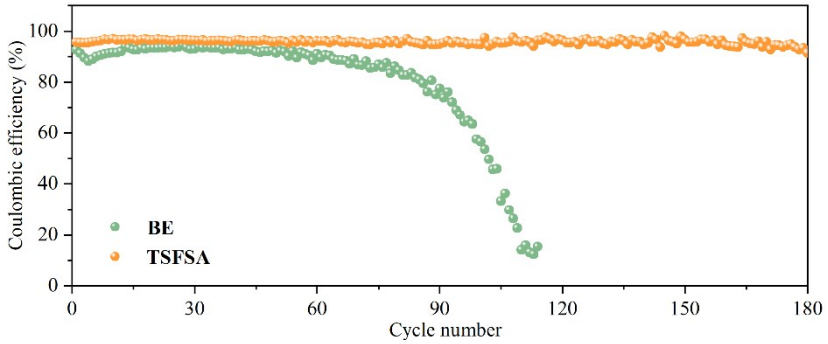

Fig. S10. Coulombic efficiency (CE) of Li||Cu half cells at a current density of 1 mA cm^{-2} and a capacity of 1 mAh cm^{-2}.

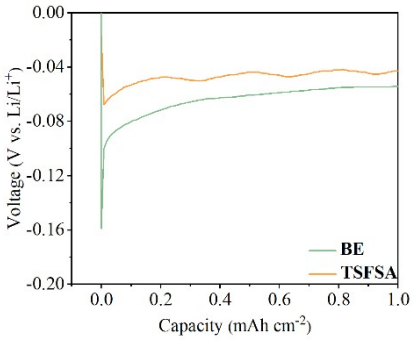

Fig. S11. Nucleation overpotential comparison of BE and TSFSA using Li||Cu half cells at a current density of 1 mA cm^{-2}.

.

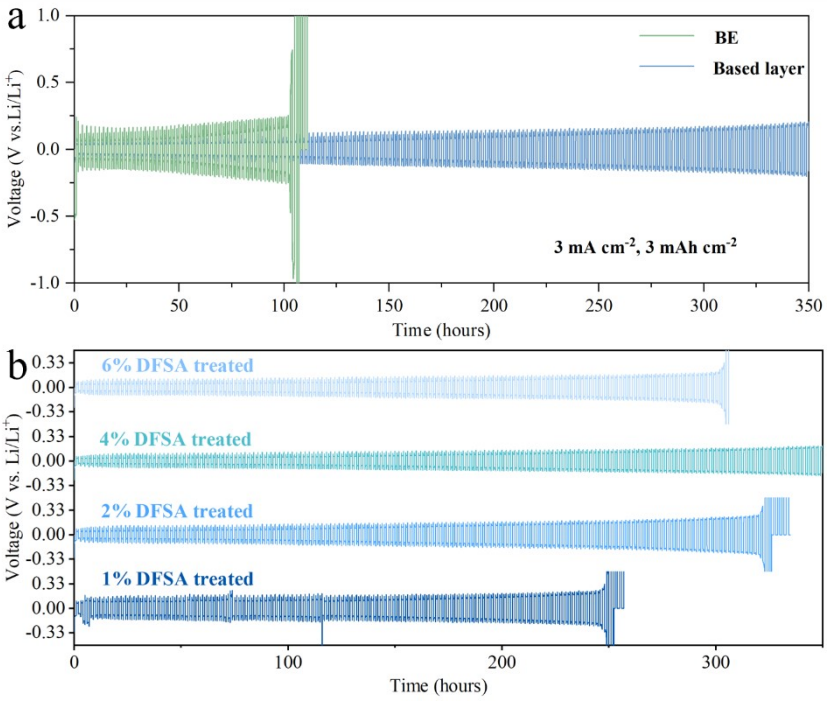

Fig. S12. (a) Cycle stability of Li||Li symmetric cells with BE and based-layer at a current density of 3 mA cm^{-2} and a capacity of 3 mAh cm^{-2}. (b) Cycle stability of Li||Li symmetric cells at a current density of 3 mA cm^{-2} and a capacity of 3 mAh cm^{-2} with different treatment concentration.

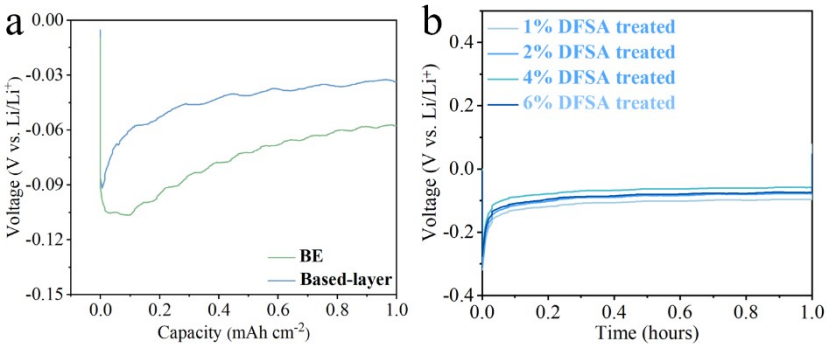

Fig. S13. (a) Nucleation overpotential comparison of BE and based-layer using Li||Li symmetric cells at a current density of 0.5 mA cm^{-2}. (b) Nucleation overpotential comparison of based-layer with different treatment concentration at a current density of 3 mA cm^{-2}.

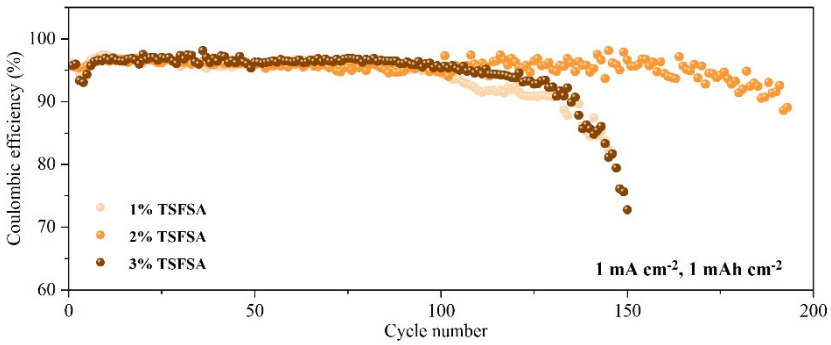

Fig. S14. Coulombic efficiency (CE) of Li||Cu half cells with different TSFSA concentration at a current density of 1 mA cm^{-2} and a capacity of 1 mAh cm^{-2}.

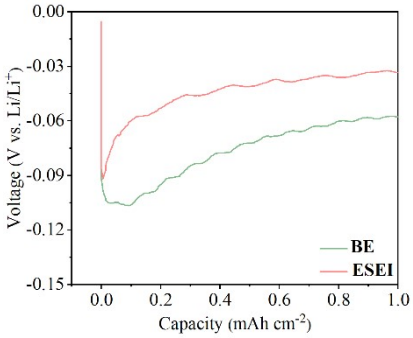

Fig. S15. Nucleation overpotential comparison of BE and ESEI using Li||Li symmetric cells at a current density of 0.5 mA cm^{-2}.

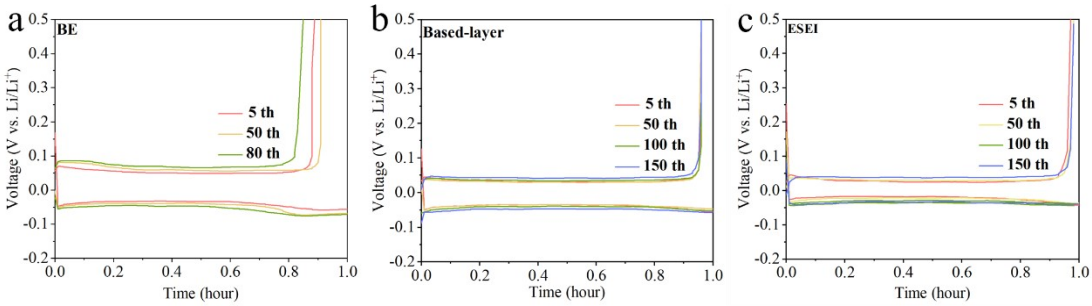

Fig. S16. Voltage-time curves of Li||Cu half cells with (a) BE, (b) based-layer and (c) ESEI.

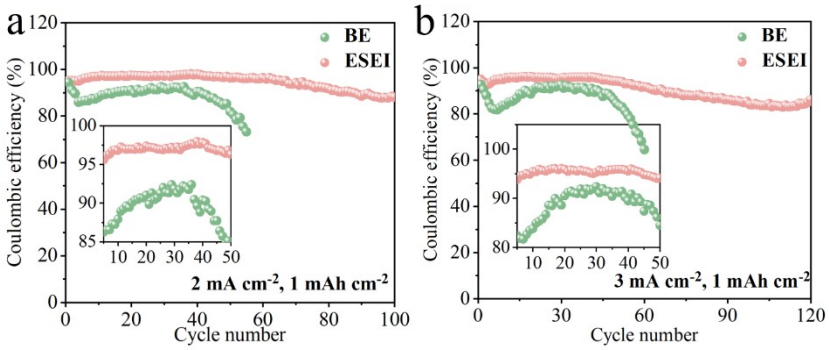

Fig. S17. The CE in BE and ESEI using Li||Cu cells of 1 mAh cm^{-2} with (a) 2 mA cm^{-2}, (b) 3 mA cm^{-2}.

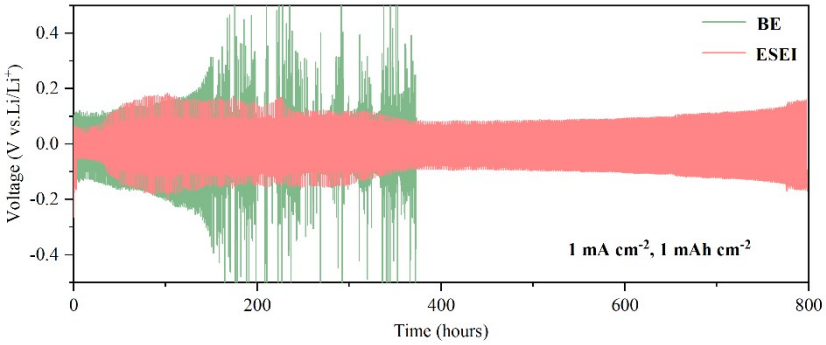

Fig. S18. Cycle stability of Li||Li symmetric cells with BE and ESEI at a current density of 1 mA cm^{-2} and a capacity of 1 mAh cm^{-2} in commercial carbonate electrolyte (1 M $LiPF_6$ in EC/EMC, v/v=3:7).

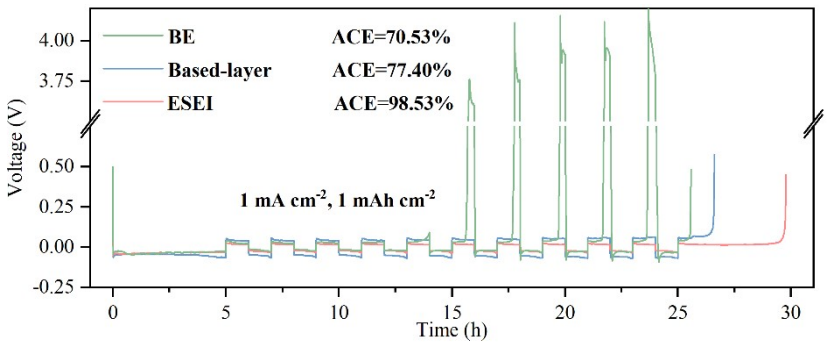

Fig. S19. Li metal plating/stripping average CE evaluated by Li||Cu half cells in commercial carbonate electrolyte (1 M $LiPF_6$ in EC/EMC, v/v=3:7).

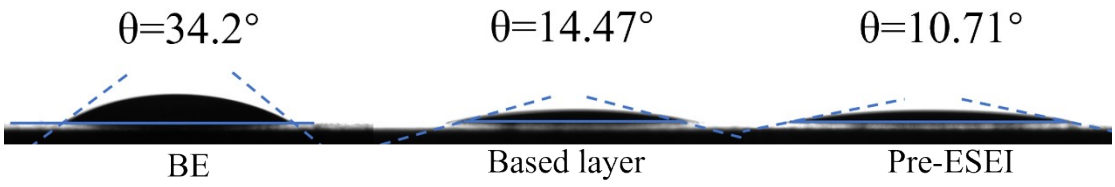

Fig. S20. Contact angle measurements of BE, based-layer and pre-ESEI.

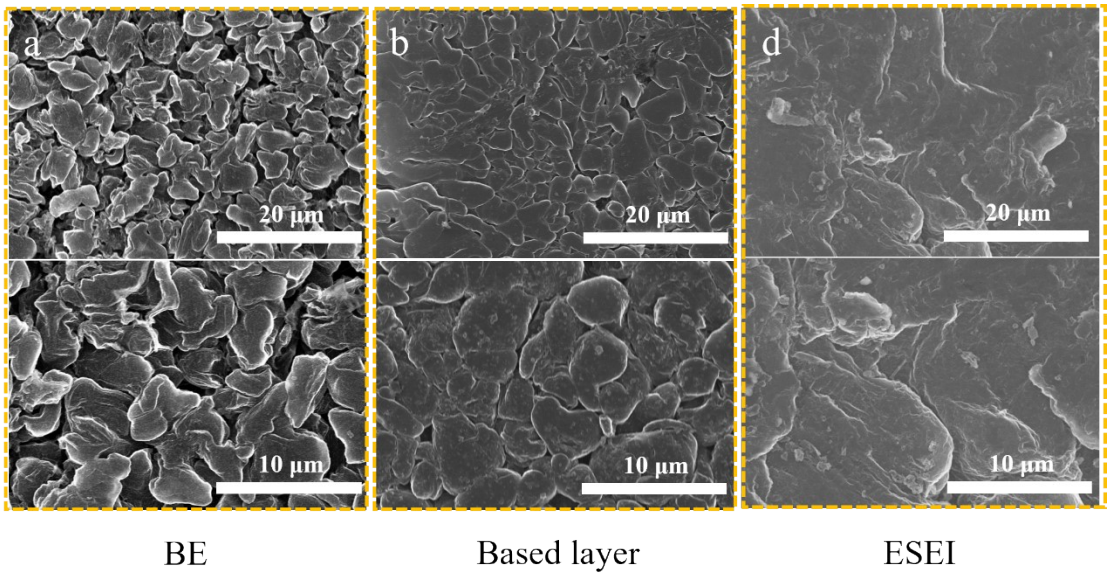

Fig. S21. SEM images of (a) BE, (b) based-layer and (c) ESEI at 10th plating.

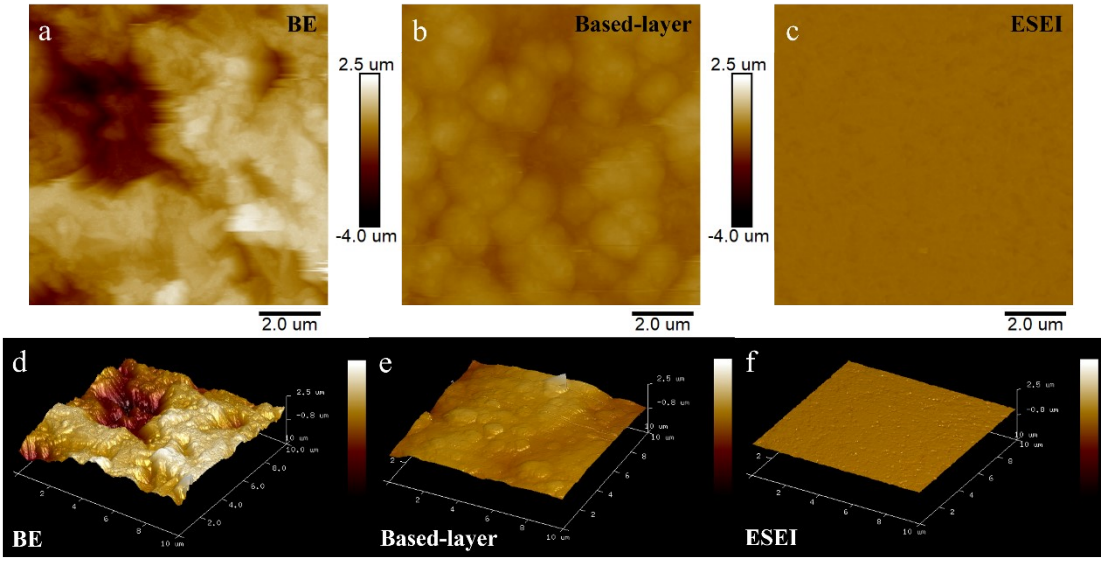

Fig. S22. AFM images of Li surface morphology at 10th plating of (a) BE (b) based-layer and (c) ESEI with an area of 10μm×10μm. The Corresponding 3D AFM model images of Li surface morphology at 10th plating of (d) BE (e) based-layer and (f) ESEI with an area of 10μm×10μm. Color bars :−4-2.5 μm.

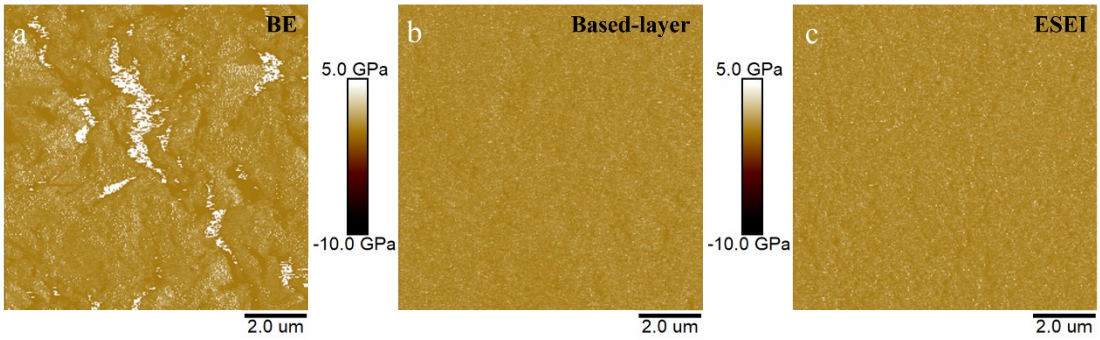

Fig. S23. The Corresponding Young's modulus mapping of (a) BE (b) based-layer and (c) ESEI with an area of 10μm×10μm. Color bars :−10-5 Gpa.

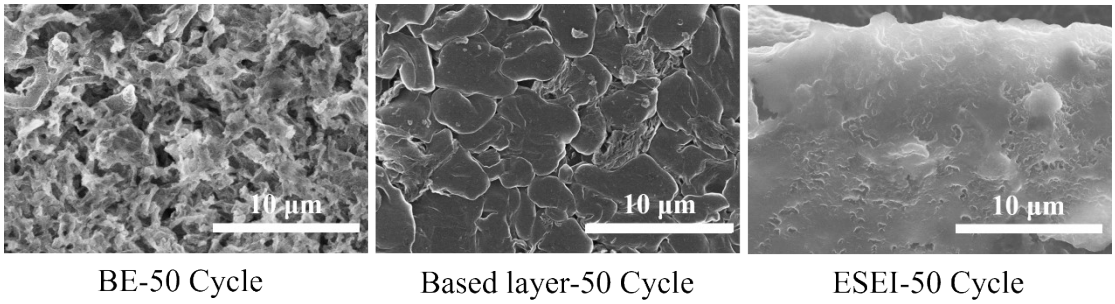

Fig. S24. SEM images of (a) BE, (b) based-layer and (c) ESEI at 50th plating.

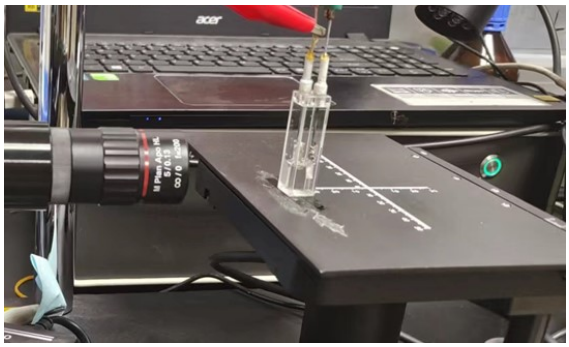

Fig. S25. In-situ optical devices for in-situ optical characterization.

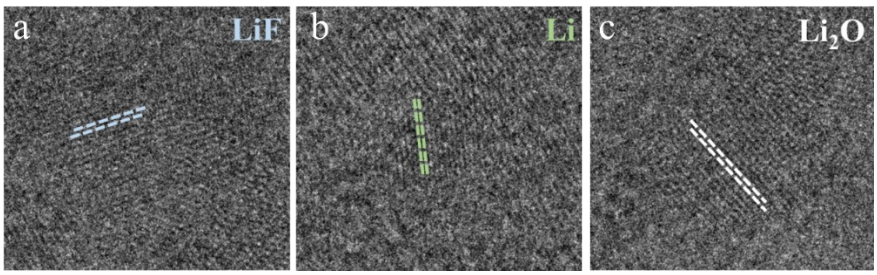

Fig. S26. The enlarged detail views of Fig. 4g.

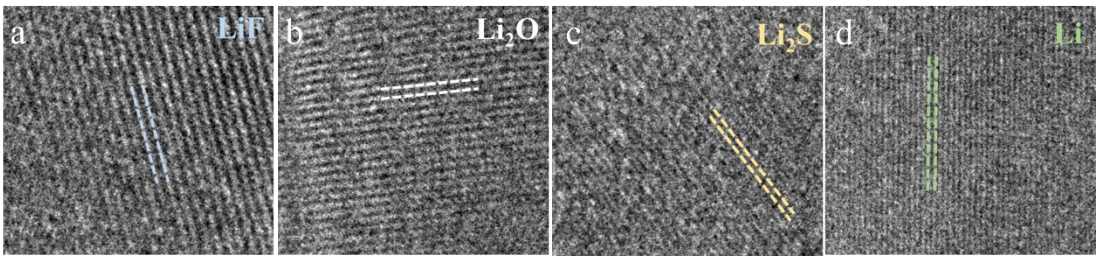

Fig. S27. The enlarged detail views of Fig. 4i.

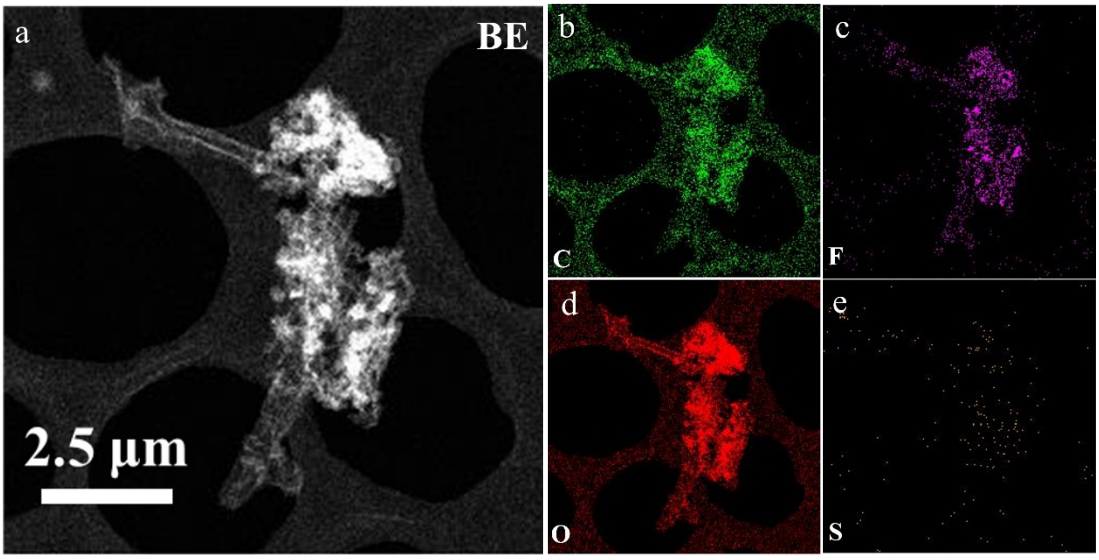

Fig. S28. The HAADF-STEM image and elemental mapping of BE in Li||Li symmetric cell after 5 cycles.

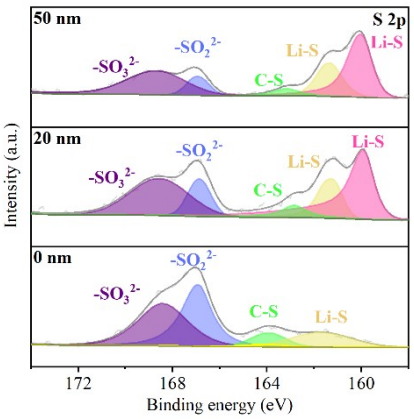

Fig. S29. XPS S 2p spectra for ESEI cycled after 5 cycles.

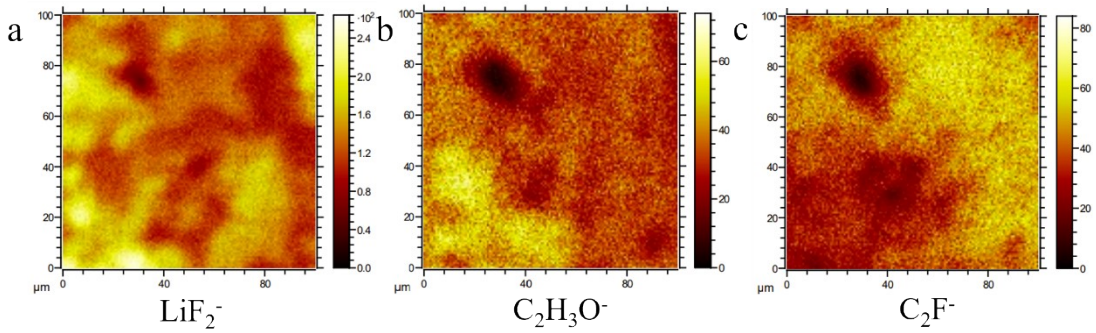

Fig. S30. TOF-SIMS mappings of the (a) LiF_2^-, (b) $C_2H_3O^-$ and (c) C_2F^- species on the surface of the cycled BE batteries.

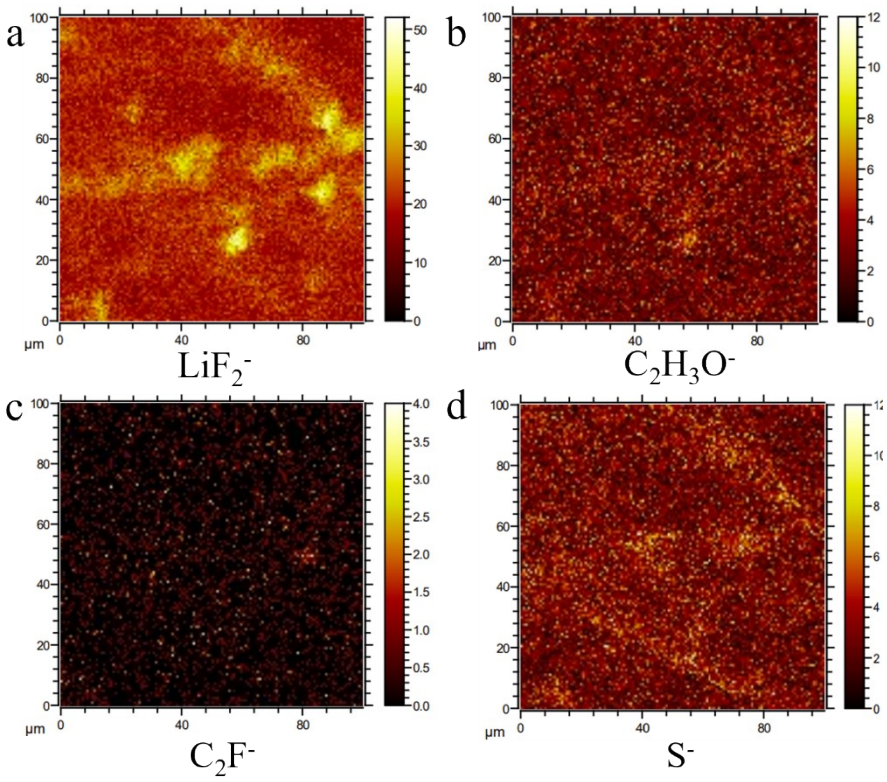

Fig. S31. TOF-SIMS mappings of the (a) LiF_2^-, (b) $C_2H_3O^-$, (c) C_2F^- and (d) S^- species on the surface of the cycled ESEI batteries.

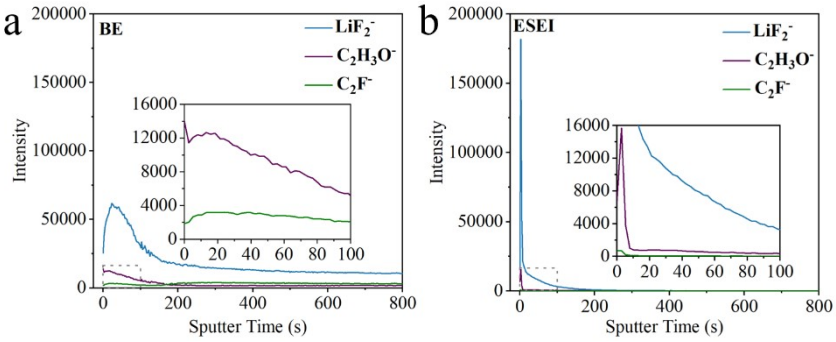

Fig. S32. The TOF-SIMS depth sputter curves of Li surface for (a) BE and (b) ESEI.

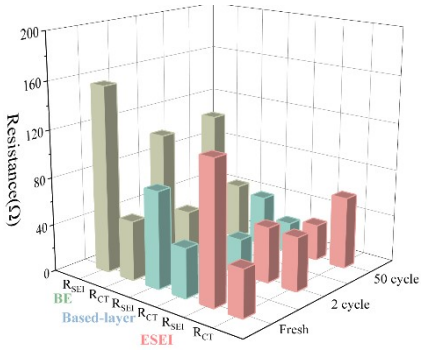

Fig. S33. The EIS fitting results of Li||Li symmetric cells.

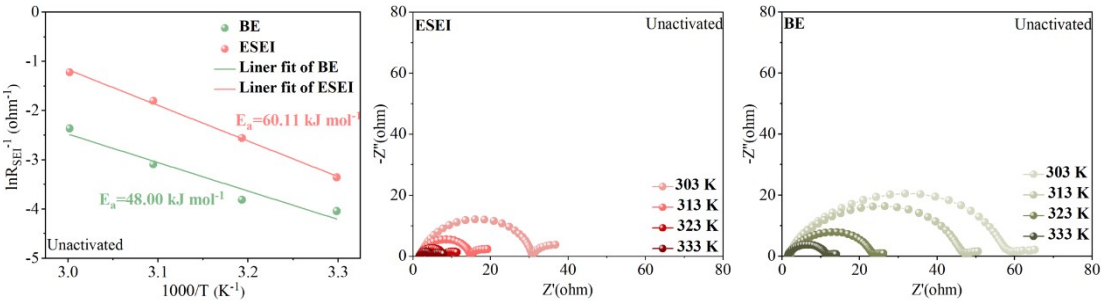

Fig. S34. (a) The Arrhenius behavior and corresponding unactivation energy for Li^+ diffusion through activated SEI film derived from R_{SEI} in Nyquist plots at various temperatures of fresh Li||Li symmetric cells with BE and ESEI. EIS plots of the Li||Li symmetric cells with (b) ESEI and (c) BE at different temperatures before cycling.

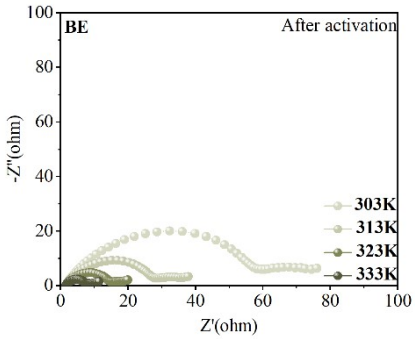

Fig. S35. EIS plots of the Li||Li symmetric cells with BE at different temperatures after cycling.

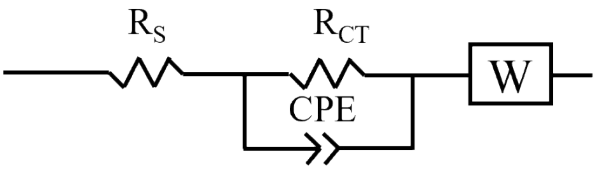

Fig. S36. The equivalent circuit used to fit the Li||Li symmetric cells.

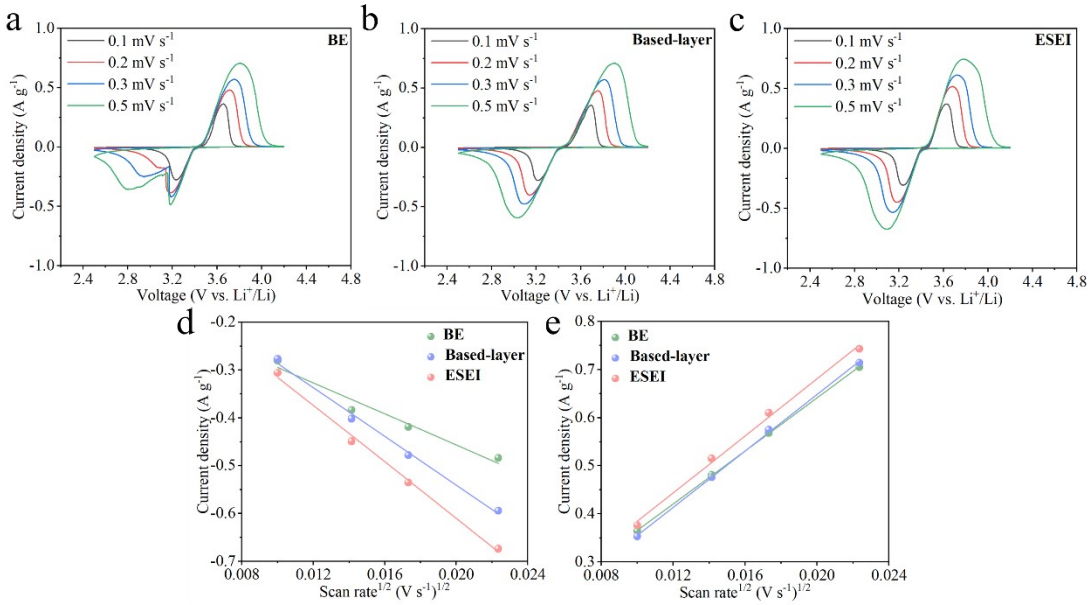

Fig. S37. The CV curves of Li||LFP full cells with (a) BE, (b) based-layer and (c) ESEI at different scan rates (0.1-0.5 mV s^{-1}) after two cycles activation. (d) Reduction peaks and (e) oxidation peaks currents against square root of scan rates for BE, Based-layer and ESEI.

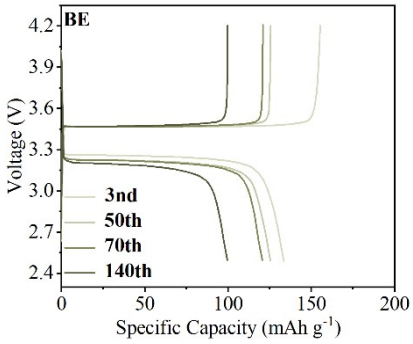

Fig. S38. Charge-discharge profiles of Li||LFP full cells with BE under a N/P of 2.98.

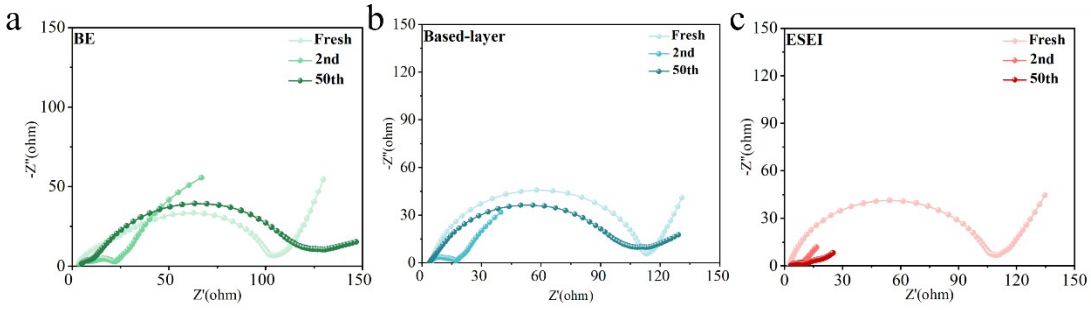

Fig. S39. Nyquist plots of Li||LFP full cells at various cycles for (a) BE, (b) based-layer and (c) ESEI.

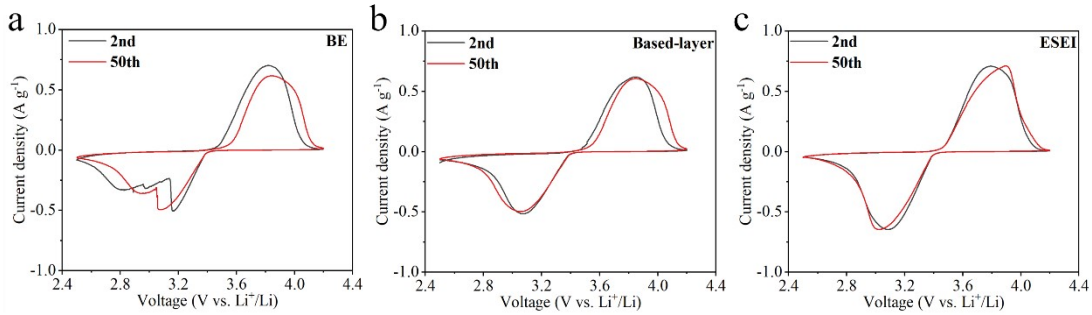

Fig. S40. The CV curves of Li||LFP full cells at two cycles activation and 50 cycles for (a) BE, (b) based-layer and (c) ESEI.

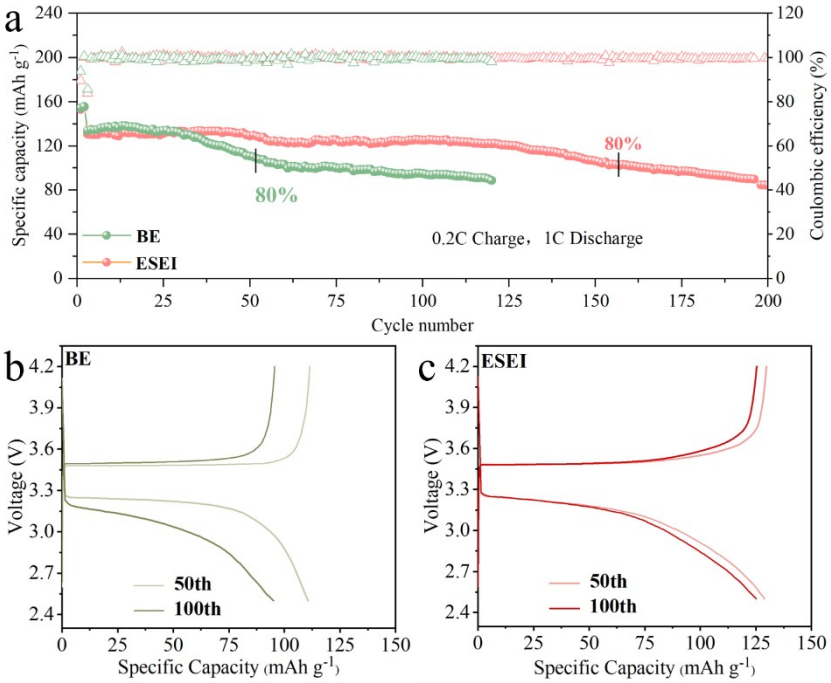

Fig. S41. (a) Long-cycling performance of the Li||LFP full cells in commercial carbonate electrolyte (1 M $LiPF_6$ in EC/EMC, v/v=3:7). The mass loading of LFP is ~20.5 mg cm^{-2} and the thickness of Li chip is 300 µm. Charge-discharge voltage profiles of the Li||LFP full cells with (b) ESEI and (c) BE. The mass loading of LFP is ~20.5 mg cm^{-2} and the thickness of Li chip is 300 µm.

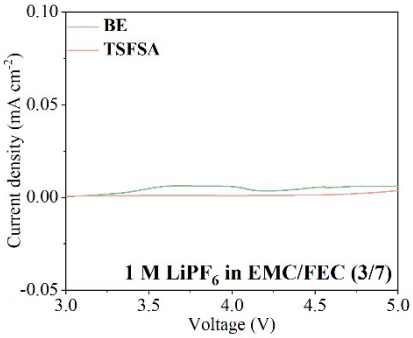

Fig. S42. The LSV curves of BE and TSFSA electrolyte with 1mV s^{-1}.

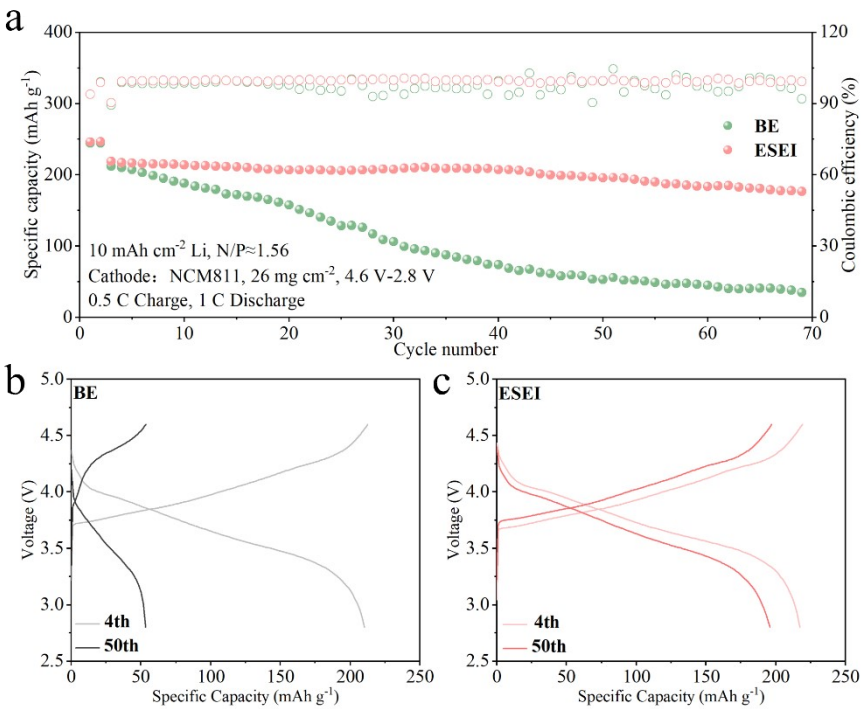

Fig. S43. (a) Long-term cycling performance of high voltage Li||NCM811 full cells with BE and ESEI in a 1 M $LiPF_6$ in FEC/EMC (v/v = 3:7) electrolyte. Conditions: 10 mAh cm^{-2} deposited Li, high area loading NCM811 (6.4 mAh cm^{-2} at 0.1C, 26 mg cm^{-2}), 2.8 V-4.6 V. The cells were activated at 0.1 C for 2 cycles, then charged at 0.5 C and discharged at 1 C in subsequent cycles (1C=200 mA g^{-1}). The corresponding charge-discharge profiles of the high voltage Li||LFP NCM811 cells with (b) BE and (c) ESEI.

Table S1. Cycling stability of ESEI compared with previously reported work.

Electrolyte	Method	Current density (mA cm^{-2})	Areal capacity (mAh cm^{-2})	Cycling time (h)	Ref.
1 M $LiPF_6$ EC/EMC+TSFSA	chemical reaction + electrochemical activation	1	1	800	This work
1 M $LiPF_6$ EMC/FEC+TSFSA	chemical reaction + electrochemical activation	1 3	1 3	2100 450	This work
1 M $LiPF_6$ EC/DEC	Artificial SEI	0.5 1	1 1	2325 850	[1]
1 M $LiPF_6$ EC/EMC/FEC	Artificial SEI	1	0.5	1200	[2]
1 M $LiPF_6$ EC/DEC	Artificial SEI	1	1	750	[3]
1 M $LiPF_6$ EC/DEC/FEC/VC	Artificial SEI	1	1	450	[4]
1 M $LiPF_6$ EC/DMC/FEC	Artificial SEI	0.5	1	950	[5]
1 M $LiPF_6$ EC/DMC	Artificial SEI	0.5	1	320	[5]
1 M $LiPF_6$ EC/DEC/FEC/VC	Artificial SEI	1 2 4	1 1 1	800 250 150	[6]
1.3 M $LiPF_6$ EC/DEC/FEC	Artificial SEI	0.5	2	800	[7]
1 M $LiPF_6$ EC/DEC/DMC	Artificial SEI	0.5	1	400	[8]
1 M $LiPF_6$ EC/DEC/FEC	Artificial SEI	1 3	1 3	400 80	[9]
1 M $LiPF_6$ EC/DEC	Artificial SEI	1 2	1 1	900 400	[10]
1 M $LiPF_6$ FEC/DMC	Artificial SEI	0.5 1	1 1	1800 800	[11]
1 M $LiPF_6$ EC/DEC/FEC	Additive	1	1	1200	[12]
1 M $LiPF_6$ EC/DEC+EITC	Additive	0.5	0.5	600	[13]
1 M $LiPF_6$ EC/EMC+TMSILN	Additive	1	1	550	[14]
1 M $LiPF_6$ EC/DMC+HFAC	Additive	1	0.5	500	[15]
1 M $LiPF_6$ EC/DEC+DETFP	Additive	2	2	250	[16]
1 M $LiPF_6$ EC/DEC/FEC+ $RbNO_3$+18-Crown-6	Additive	1 3	1 1	250 140	[17]
1 M $LiPF_6$ EC/DEC+ KSeCN	Additive	1	3	120	[18]
1 M $LiPF_6$ EC/DMC/FEC +DIDP+TMSF+ $LiNO_3$	Additive	1	1	500	[19]

Table S2. AFM characterization of average root-mean-square roughness at 10th plating of BE, Based-layer and ESEI with an area of 10μm×10μm.

Average roughness	BE (nm)	Based-layer (nm)	ESEI (nm)
R_q	718.0	217.0	30.1
R_a	561.0	176.0	22.6

Table S3. The specific values of R_{SEI} of Li||Li symmetric cells at various temperatures for BE with unactivated.

T (K)	R_{SEI} (Ω)	ln (1/ R_{SEI})	1000/T (K^{-1})
303	56.89	-4.04107	3.2987
313	45.35	-3.81441	3.19336
323	22.06	-3.09377	3.09454
333	10.63	-2.36368	3.00165

Table S4. The specific values of R_{SEI} of Li||Li symmetric cells at various temperatures for ESEI with unactivated.

T (K)	R_{SEI} (Ω)	ln (1/ R_{SEI})	1000/T (K^{-1})
303	28.68	-3.35634	3.2987
313	12.90	-2.55754	3.19336
323	6.06	-1.80171	3.09454
333	3.40	-1.22378	3.00165

Table S5. The specific values of R_{SEI} of Li||Li symmetric cells at various temperatures for BE with activated.

T (K)	R_{SEI} (Ω)	ln (1/ R_{SEI})	1000/T (K^{-1})
303	58.44	-4.06800	3.2987
313	27.33	-3.30798	3.19336
323	13.91	-2.63261	3.09454
333	6.40	-1.85630	3.00165

Table S6. The specific values of R_{SEI} of Li||Li symmetric cells at various temperatures for ESEI with activated.

T (K)	R_{SEI} (Ω)	ln (1/ R_{SEI})	1000/T (K^{-1})
303	24.88	-3.21406	3.2987
313	11.96	-2.48157	3.19336
323	6.59	-1.88555	3.09454
333	3.22	-1.16938	3.00165

Table S7. Full cells of ESEI compared with previously reported work.

Capacity (mAh cm^{-2})	Cycle Life	Electrolyte	Strategy	Charge C-rate	Discharge C-rate	N/P	Ref.
3.49	160	1 M $LiPF_6$ EC/EMC+TSFSA	Chemical reaction + electrochemical activation	C/5	1 C	~17	This work
3.49	115 260	1 M $LiPF_6$ EMC/FEC +TSFSA	Chemical reaction + electrochemical activation	C/2 C/5	C/2 1 C	0.89 2.98	This work
6.4	70	1 M $LiPF_6$ EMC/FEC +TSFSA	Chemical reaction + electrochemical activation	0.5 C	1 C	1.56	This work
1.60	150	1M $LiPF_6$ EC/DEC	Artificial SEI	1 C	1 C	>30	[1]
4	300	1 M $LiPF_6$ EC/EMC/FEC	Artificial SEI	C/5	1 C	2.5	[2]
0.76	300	1 M $LiPF_6$ EC/DEC/FEC/VC	Artificial SEI	1 C	1 C	5.26	[6]
3	50	1M $LiPF_6$ EC/DEC/FEC	Artificial SEI	C/3	C/3	1	[20]
3.67	100	1M $LiPF_6$ EC/DEC/EMC	Artificial SEI	C/5	1 C	2.72	[21]
2.5	250	1M $LiPF_6$ EC/DEC/FEC	Artificial SEI	C/5	C/3	4	[22]
1.72	200	1 M $LiPF_6$ EC/DMC/FEC +DIDP+TMSF+ $LiNO_3$	Additive	1 C	1 C	>100	[19]
3.4	200	1 M $LiPF_6$ FEC/DMC+$LiNO_3$+TPFPB	Additive	C/3	C/3	2.71	[23]
2.5	200	1 M $LiPF_6$ FEC/DMC+$LiNO_3$+DMSO	Additive	C/2	C/2	4	[24]
4.0	100	1M $LiPF_6$ EC/DMC/EMC	Artificial SEI	0.5 C	0.5 C	2.49	[25]
3.5	180	1.0 M LiTFSI DOL/DME+$LiNO_3$	Artificial SEI	0.3 C	0.3 C	2.33	[26]
2.5	220	1.5 M LiTFSI DME+ $LiNO_3$+ $CsNO_3$	Additive	1 C	1 C to 2 C	2	[27]
2.55	75	LiFSI-PES=1:2.5 (mol.)	Electrolyte	5 C	5 C	2.5	[28]
2.5	150	1 M $LiPF_6$ EC/DEC/FEC+40% 3 M TMP/$LiNO_3$	Electrolyte	0.2 C	0.2 C	5	[29]

References

1. R. Pathak, K. Chen, A. Gurung, K. M. Reza, B. Bahrami, J. Pokharel, A. Baniya, W. He, F. Wu, Y. Zhou, K. Xu and Q. Qiao, *Nature Communications*, 2020, **11**, 93.
2. Y. Xie, Y. Huang, Y. Zhang, T. Wu, S. Liu, M. Sun, B. Lee, Z. Lin, H. Chen, P. Dai, Z. Huang, J. Yang, C. Shi, D. Wu, L. Huang, Y. Hua, C. Wang and S. Sun, *Nature Communications*, 2023, **14**, 2883.
3. J. Pokharel, A. Cresce, B. Pant, M. Y. Yang, A. Gurung, W. He, A. Baniya, B. S. Lamsal, Z. Yang, S. Gent, X. Xian, Y. Cao, W. A. Goddard, 3rd, K. Xu and Y. Zhou, *Nature communications*, 2024, **15**, 3085-3085.
4. S. Ni, M. Zhang, C. Li, R. Gao, J. Sheng, X. Wu and G. Zhou, *Advanced Materials*, 2023, **35**, e2209028.
5. Z. Peng, J. Song, L. Huai, H. Jia, B. Xiao, L. Zou, G. Zhu, A. Martinez, S. Roy, V. Murugesan, H. Lee, X. Ren, Q. Li, B. Liu, X. Li, D. Wang, W. Xu and J.-G. Zhang, *Advanced Energy Materials*, 2019, **9**, 1901764.
6. S. Fang, F. Wu, S. Zhao, M. Zarrabeitia, G.-T. Kim, J.-K. Kim, N. Zhou and S. Passerini, *Advanced Energy Materials*, 2023, **13**, 2302577.
7. S. Sun, S. Myung, G. Kim, D. Lee, H. Son, M. Jang, E. Park, B. Son, Y.-G. Jung, U. Paik and T. Song, *Journal of Materials Chemistry A*, 2020, **8**, 17229-17237.
8. D. Kang, N. Hart, J. Koh, L. Ma, W. Liang, J. Xu, S. Sardar and J. P. Lemmon, *Energy Storage Materials*, 2020, **24**, 618-625.
9. D. Lee, S. Sun, H. Park, J. Kim, K. Park, I. Hwang, Y. Jung, T. Song and U. Paik, *Journal of Power Sources*, 2021, **506**, 230158.
10. Y. Wang, F. Liu, G. Fan, X. Qiu, J. Liu, Z. Yan, K. Zhang, F. Cheng and J. Chen, *Journal of the American Chemical Society*, 2021, **143**, 2829-2837.
11. X. Li, M. Lv, Y. Tian, L. Gao, T. Liu, Q. Zhou, Y. Xu, L. Shen, W. Shi, X. Li, Y. Lu, X. Liu and S. Xiao, *Nano Energy*, 2021, **87**, 106214.
12. Y. Qin, H. Wang, J. Zhou, R. Li, C. Jiang, Y. Wan, X. Wang, Z. Chen, X. Wang, Y. Liu, B. Guo and D. Wang, *Angewandte Chemie-International Edition*, 2024, DOI: 10.1002/anie.202402456.
13. J. Zhang, X. Yue, Z. Wu, Y. Chen, Y. Bai, K. Sun, Z. Wang and Z. Liang, *Nano Letters*, 2023, **23**, 9609-9617.
14. V. A. K. Adiraju, O. B. Chae, J. R. Robinson and B. L. Lucht, *Acs Energy Letters*, 2023, **8**, 2440-2446.
15. F. Li, J. Liu, J. He, Y. Hou, H. Wang, D. Wu, J. Huang and J. Ma, *Angewandte Chemie-International Edition*, 2022, **61**, e202205091.
16. P. Zhou, Y. Xia, W.-h. Hou, S. Yan, H.-Y. Zhou, W. Zhang, Y. Lu, P. Wang and K. Liu, *Nano Letters*, 2022, **22**, 5936-5943.
17. S. Gu, S.-W. Zhang, J. Han, Y. Deng, C. Luo, G. Zhou, Y. He, G. Wei, F. Kang, W. Lv and Q.-H. Yang, *Advanced Functional Materials*, 2021, **31**, 2102128.
18. A. Fu, J. Lin, Z. Zhang, C. Xu, Y. Zou, C. Liu, P. Yan, D.-Y. Wu, Y. Yang and J. Zheng, *Acs Energy Letters*, 2022, **7**, 1364-1373.
19. Y. Gao, G. Wu, W. Fang, Z. Qin, T. Zhang, J. Yan, Y. Zhong, N. Zhang and G. Chen, *Angewandte Chemie-International Edition*, 2024, DOI: 10.1002/anie.202403668.
20. S. Stalin, P. Chen, G. Li, Y. Deng, Z. Rouse, Y. Cheng, Z. Zhang, P. Biswal, S. Jin, S. P. Baker, R. Yang and L. A. Archer, *Matter*, 2021, **4**, 3753-3773.

21. S. Li, J. Huang, Y. Cui, S. Liu, Z. Chen, W. Huang, C. Li, R. Liu, R. Fu and D. Wu, *Nature Nanotechnology*, 2022, **17**, 613-621.
22. Z. Huang, J.-C. Lai, S.-L. Liao, Z. Yu, Y. Chen, W. Yu, H. Gong, X. Gao, Y. Yang, J. Qin, Y. Cui and Z. Bao, *Nature Energy*, 2023, **8**, 577-585.
23. S. Li, W. Zhang, Q. Wu, L. Fan, X. Wang, X. Wang, Z. Shen, Y. He and Y. Lu, *Angewandte Chemie-International Edition*, 2020, **59**, 14935-14941.
24. S. Liu, X. Ji, N. Piao, J. Chen, N. Eidson, J. Xu, P. Wang, L. Chen, J. Zhang, T. Deng, S. Hou, T. Jin, H. Wan, J. Li, J. Tu and C. Wang, *Angewandte Chemie-International Edition*, 2021, **60**, 3661-3671.
25. H. Dai, J. Dong, M. Wu, Q. Hu, D. Wang, L. Zuin, N. Chen, C. Lai, G. Zhang and S. Sun, *Angewandte Chemie-International Edition*, 2021, **60**, 19852-19859.
26. T. D. Pham, A. Bin Faheem, J. Kim, K. Kwak and K.-K. Lee, *Advanced Functional Materials*, 2023, **33**, 2305284
27. M. M. Rahman, S. Tan, Y. Yang, H. Zhong, S. Ghose, I. Waluyo, A. Hunt, L. Ma, X.-Q. Yang and E. Hu, *Nature Communications*, 2023, **14**, 8414.
28. J. Yu, X. Ma, X. Zou, Y. Hu, M. Yang, J. Yang, S. Sun and F. Yan, *Energy & Environmental Science*, 2024, **17**, 4519-4530.
29. Z. Wang, Y. Wang, B. Li, J. C. Bouwer, K. Davey, J. Lu and Z. Guo, *Angewandte Chemie-International Edition*, 2022, **61**, e202206682.